

AEROELASTIC DESIGN OF A STRUT-BRACED DRY WING FOR A HYDROGEN AIRCRAFT IN AN MDO FRAMEWORK

Charly Mollet[1], Lander Vertonghen[2] & Cédric Julien[2]

[1]DAAA, ONERA, Institut Polytechnique de Paris, 92320, Châtillon, France
[2]DMAS, ONERA, Université Paris-Saclay, 92320, Châtillon, France

Abstract

This paper presents the conceptual aero-structural design of a LH2-powered Strut-Braced Dry Wing (SBDW) aircraft developed within the Clean Aviation UPWing project for a Short-Medium Range mission (239 passengers, 2500 Nm). This work investigates how energy consumption can be reduced through LH2 propulsion and Ultra High Aspect Ratio Wing (UHARW) configurations. A global Multi-disciplinary Design Optimization (MDO) process is implemented, combining aerodynamic, structural, and Overall Aircraft Design (OAD) studies through a surrogate model approach. The structural study demonstrates how the addition of a strut influences the structural design through key parameters such as the relative wing-strut sweep for example. Essential geometry adaptations, including a double-tapered wing, are proposed to ensure sufficient structural inertia at the wing-strut junction to sustain aerodynamic loads.
This global process has resulted in an aircraft configuration with an aspect ratio of 22.91 which has been designed for 1g, -1g and 2.5g design load cases and checked for flutter. Moreover, an aeroelastic optimization process has been developed to obtain more realistic aeroelastic loads for the design by accounting for the wing flexibility in the loads calculation.
Future work will focus on this aeroelastic optimization to refine the optimal configuration design and a high-fidelity CFD-structural coupling is to be performed for validation and performance evaluation.

Keywords: Strut-Braced Wing, LH2 powered aircraft , Ultra High Aspect Ratio Wing, Optimization, Aeroelasticity, Aircraft Structural Design.

1. General Introduction

In the context of reducing the environmental impact of aviation, future aircraft should further improve their fuel efficiency and reduce carbon emissions. Nowadays, kerosene-powered aircraft seem close to their optimal performance. Thus, innovative aircraft configurations and new fuel possibilities are more and more under study. The Clean Aviation UPWing project work package WP2.2 - conducted jointly by ONERA, Delft University of Technology, and the University of Stuttgart - focuses mainly on the study of a LH2 powered aircraft with an ultra high aspect ratio wing (UHAR) for a Short-Medium-Range like mission (2500 Nm, 239 PAX, Cruise Mach number: 0.78).
The main goal is to investigate how the energy consumption may be reduced by using LH2 propulsion and by increasing the wing efficiency. Improvements in efficiency include the use of ultra high aspect ratio wings (UHAR) which requires novel approaches to be able to sustain the aerodynamic loads. Ma and Elham [1] propose a review of concepts that are studied to tackle this issue with solutions going from redesigned cantilever wings to strut/truss-braced wings and twin fuselage aircraft. As a continuation of the U-HARWARD project [2], the Strut-Braced Wing (SBW) configuration has been selected to design a structurally viable UHARW.
However, this approach challenges the structural knowledge on cantilever wings. In fact, the strut-wing system is inherently hyperstatic and the presence of a strut introduces additional bending moment components and new critical design locations especially near the strut-wing junction. So the

problem can no longer be modeled simply as a minimization of the lift bending moment but should also consider the in-plane bending moment and the compressive forces that the strut introduces in the wing. The strut itself must as well be designed to avoid buckling under negative loads.

This paper details the approach used to bring the consideration of these structural and also aeroelastic issues into a global surrogate model that combines aerodynamic, structural and overall aircraft design (OAD) studies. The global process consists in implementing a Design of Experiments (DoE) collecting evaluations of a wide range of aircraft configurations from both structural and aerodynamic calculations. These results are then used to build a set of disciplinary surrogate models, leading after optimization to the selection of an optimal configuration [3].
First, the aero-structural modelling of this double-tapered wing and its impact on the DoE parameters are presented. The overall structural and aeroelastic process along with the selected load cases - used to find the design minimizing the weight of each aircraft - are also detailed. An aerodynamic implementation for the definition of the jig shape and flutter calculations are described.
Then, the resulting configuration from an optimization performed on the disciplinary surrogate models, including the structural optimization, is addressed. This 22.91 aspect ratio (AR) aircraft has a strut which is attached near the middle of the half span to sustain the loads without buckling and is located almost beneath the wing to avoid in-plane bending issues. The wing design underlines that the strut-wing junction is a key point for the structural optimization as the maximum internal loading appears here. A flutter analysis has also been performed with the optimized structure, and shows no flutter within the flight envelope.
Finally, the set-up and improvements planned for the aeroelastic design are detailed. The influence of downwash correction on the wing load was studied and it led to a method for designing the twist downwash correction to be applied to reach a design target twist law in cruise conditions.

2. Methodology

2.1 MDO Framework

The structural and aeroelastic optimizations presented in this paper are part of a global Multi-disciplinary Design Optimization (MDO) framework set up to find the best aircraft configuration for a LH2 powered aircraft with a ultra high aspect ratio (UHAR) wing for a Short-Medium-Range like mission (2500 Nm, 239 PAX, Cruise Mach number: 0.78).

The chosen solution to design an UHAR wing and still support the aircraft weight is to design a Strut-Braced Wing (SBW). To explore the design space offered by this geometry, a multi-disciplinary Design of Experiments (DoE) is computed using a set of selected global design variables defining the design space. Those global parameters are displayed in Table 1 and illustrated in Figure 1.

Part	Design Variables	Range
WING	Aspect Ratio AR	15 - 28
	Wing sweep at 25% chord (°)	20.0 - 27.5
	Root relative thickness $t/c_{\text{wing root}}$	10 % - 13 %
	Kink relative thickness $t/c_{\text{wing kink}}$	10 % - 13 %
STRUT	Relative thickness t/c_{strut}	10 % - 13 %
	Root chord $c_{\text{strut root}}$ (m)	1 - 4
	Wing/Strut junction Y_{strut} (% wing semi-span)	30 % - 60 %
	Wing/Strut relative sweep angle (% wing sweep angle)	10 % - 100 %
LOAD	Load alleviation factor LAF	0.001 - 0.3

Table 1 – Global DoE variables

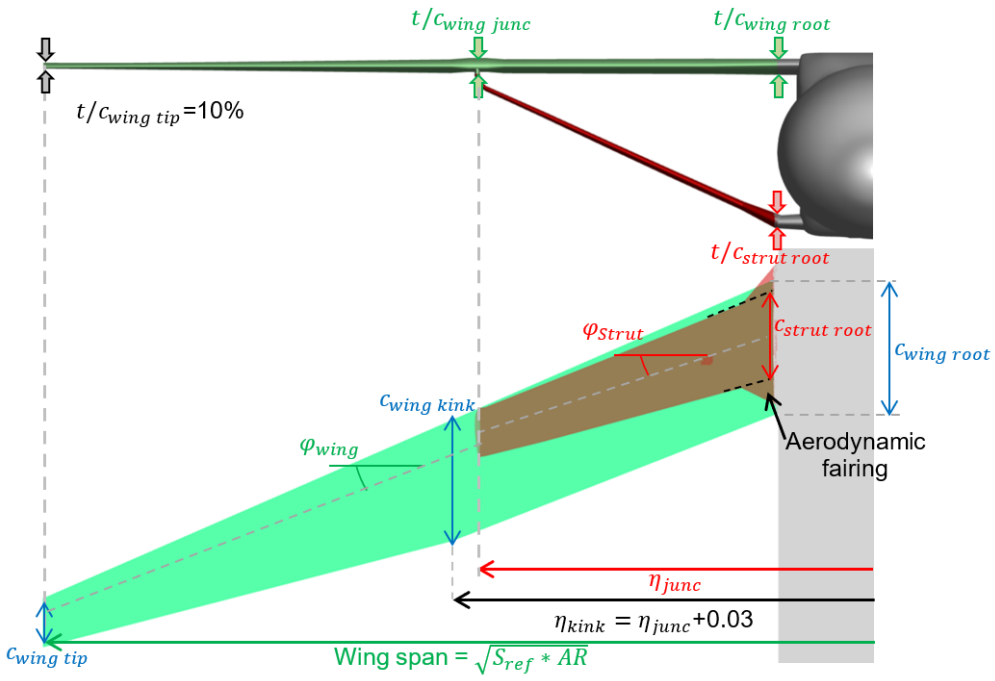
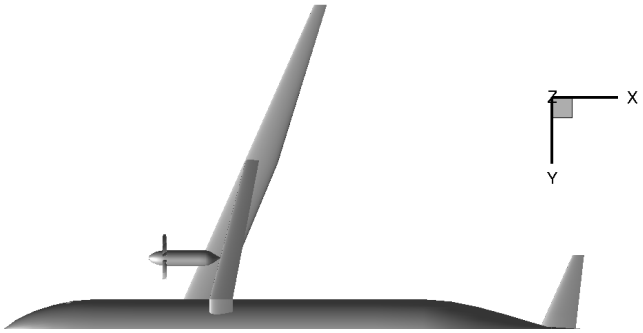


Figure 1 – Definition of the global DoE variables

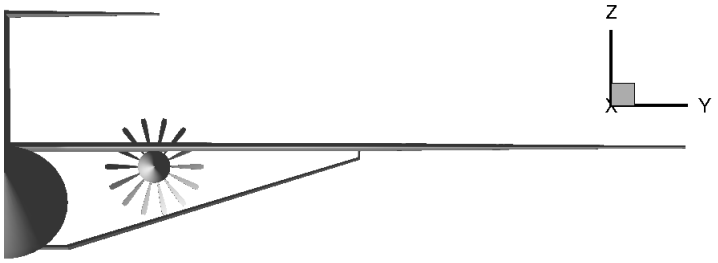
Then, each point (i.e. aircraft configuration using a combination of the above design variables values) is evaluated using Computational Fluid Dynamics (CFD) for the aerodynamic performance, while the primary wing and strut mass are obtained from a structural optimization. From these results, a surrogate model is built to interpolate between the computation points and provide a map of the design space [3].

This design space includes the first structural results detailed in Section 2.3. The wing geometry was designed to include a double taper to increase the structure inertia at the strut-wing junction to resist structural lift bending and some key design parameters are considered in the design space such as the wing-strut relative sweep (0% means the strut is perpendicular to the fuselage and 100% is for a perfectly aligned strut under the wing) [4].

An example of a configuration point from this DoE is displayed in Figure 2.



(a) Bottom view



(b) Rear view

Figure 2 – Illustration of an half aircraft from the MDO process

This external geometry is then sliced to build a structural model defining all of the wingbox components.

2.2 Structural modelling

The structural model is assembled using the data provided by the surrogate model to build the CAD model external geometry and the mass model for every configuration issued from the DoE. This procedure is interfaced with the Python API of FreeCAD. The generation of the internal structure of the wing is based on the slicing of this simplified CAD model of the wing. The wingbox is constituted of ribs, spars, skins modelled as shell elements, and stringers modelled as T-shaped beams in MSC NASTRAN.
The strut is modelled the same way as the wing but without stringers as the strutbox would not be large enough to fit them. It is clamped both at the fuselage and wing junction to reduce its buckling length. The vertical elbow at the strut-wing junction is assumed to be rigid and so is the horizontal section that links the strut root to the fuselage.

The structural optimization of the wing is performed within the MSC NASTRAN suite. The following optimization problem is solved to minimize the Operational Weight Empty (OWE):

$$\min_{\substack{\{\{t_{ribs}\},\{t_{spars}\},\{t_{skins}\},\{t_{stringers}\}\}_{wing} \\ \{\{t_{ribs}\},\{t_{spars}\},\{t_{skins}\}\}_{strut}}} \text{OWE}(\{t\}) \qquad \text{s.t.} \quad \begin{cases} \text{stress constraints} : \sigma(\{t\}) \leq \dfrac{\sigma_{max}}{\text{SF}}, \\ \text{buckling constraints} : \lambda(\{t\}) \geq \lambda_{min} * \text{SF}, \\ t_i \in [t_{\min}, t_{\max}]. \end{cases} \tag{1}$$

For each bay, i.e. the space between two consecutive ribs, the design variables are the thicknesses of the upper and lower skins $t_{upper\ skin}$ & $t_{lower\ skin}$, the thicknesses of the spars t_{spar} and ribs t_{rib} for both wing and strut.
On the wing only, upper and lower stringers are designed using the thickness of their flange (identical to the web thickness) $t_{upper\ stringers}$ & $t_{lower\ stringers}$. The thickness-to-height ratio for the stringers is fixed

to 5.

The material used is a 'black aluminium' isotropic material equivalent to a quasi-isotropic carbon composite layup material whose properties are: E = 57.24 GPa, G = 21.84 GPa, ν = 0.31 and a yield strength σ_{max} = 200 MPa [5]. The buckling limit λ_{min} is fixed at 1 and the safety factor SF at 1.5.

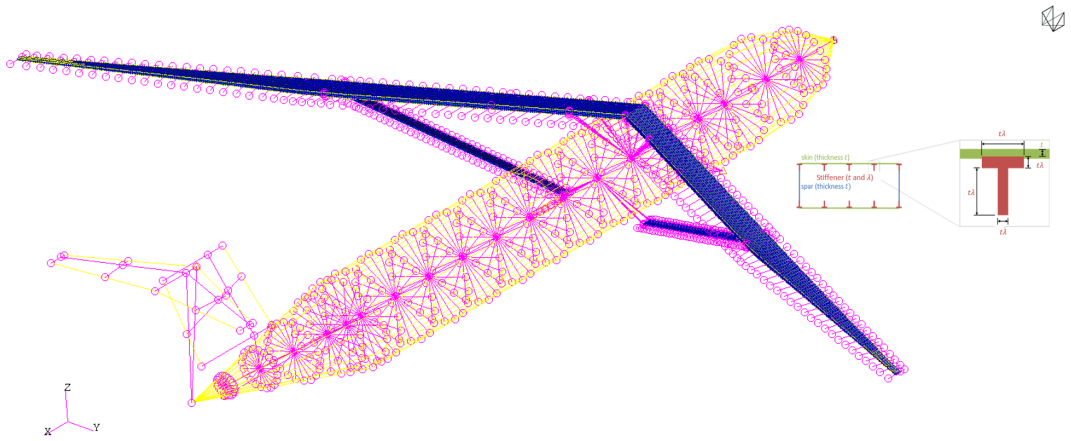


Figure 3 – Illustration of the MSC Nastran structural model used for the design

2.3 Strut influence on the design

With the aim of minimizing induced drag, a trend of increasing AR is noticeable in the aircraft industry. However, cantilever wings with ultra high aspect ratios may not sustain the critical aerodynamic loads. So a possibility to relieve the wing from a part of these loads is to add a strut. Other concepts such as truss-braced wing or twin-fuselage aircraft have also been explored [1].
The effect of the strut is mainly to reduce the wing root lift bending moment as shown in Figure 4 [6]. The maximum of this bending moment's location can then be shifted from the wing root on a cantilever wing to the strut-wing junction depending on its placement. In that case, if the structural inertia around the strut attachment is too small, the resulting bending stress could exceed the allowable limits. That is why the taper of the inner wing section has been fixed at a high value to ensure enough bending inertia remains until the strut-wing junction.

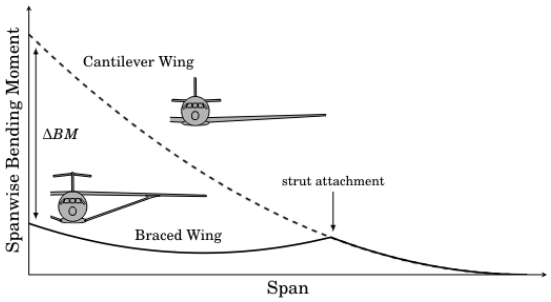


Figure 4 – Qualitative comparison of the spanwise bending moment distribution for a braced and cantilevered wing [6]

Nevertheless, the strut itself may also be confronted to high compressive loading, especially under -1g loadcase and be prone to buckling (see Figure 5). To reduce the buckling length of the strut, clamped boundary conditions were selected at both ends but a jury strut might be needed if buckling remains an issue in the design.
Moreover, as the wing and strut form a hyperstatic system, the stiffness ratio between both components influence the load transfer and subsequently the mechanical response. It is thus essential to design both the wing and strut together and consider both skin and global buckling in the optimization

process.

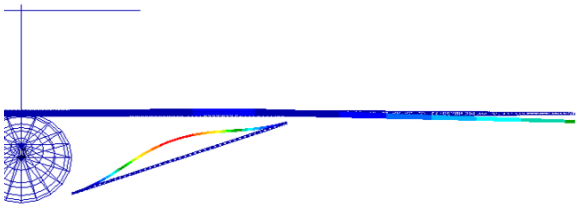
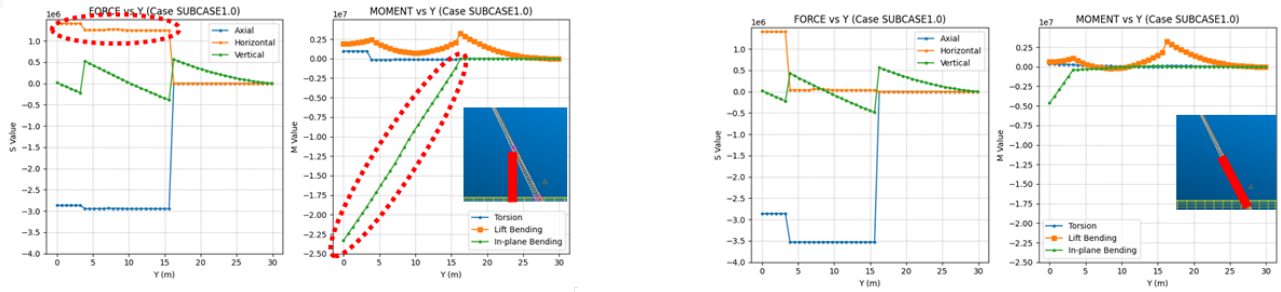


Figure 5 – Example of the first strut buckling mode under -1g load case

The strut also has another side effect on the structural design of this hyperstatic system. Indeed, it may introduce an extra in-plane bending moment that can become critical for the design if not perfectly aligned under the wing as shown by Figure 6.



(a) Strut perpendicular to the fuselage

(b) Strut aligned under the wing

Figure 6 – Force and Moment diagrams for two strut placements under the same wing

For a given wingbox, the worst stress σ_{worst} under a positive loadcase is obtained for:

$$\sigma_{worst} = \frac{F_{axial}}{A} + \frac{M_x \, z_{top}}{I_{xx}} + \frac{M_z \, x_{TE}}{I_{zz}} \tag{2}$$

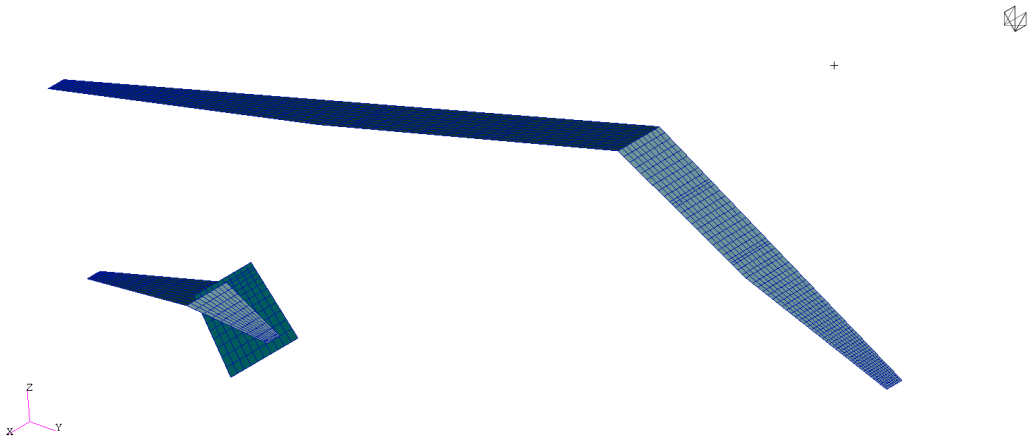
where M_x, M_z, I_{xx}, I_{zz} are the internal moments and inertias around the local x and z axes. A is the cross-section area. z_{top} and x_{TE} are the distances of the upper skin and rear spar to the elastic axis. For conventional cantilever beams, the main contribution comes from the lift bending (the second component in equation 2). However, the hyperstatic system composed of the wing and the strut highly depends on the wing-strut stiffness-ratio. This system will always introduce axial load and a relatively significant in-plane bending on the wing depending on the geometry.
Figure 6a shows the internal efforts and moments (which depend on the wing-strut stiffness ratio) for a given configuration with fixed shape and properties. When the strut is perpendicular to the fuselage, for a positive loadcase, it pulls the wing not only down but also backwards.
For this configuration with a perpendicular strut, the induced in-plane bending moment introduces higher stresses at the rear spar between the wing root and the strut junction. The contribution of this moment to the maximum stress appears to be around 3.6 times more important than the contribution of the lift bending for a configuration optimized only for lift bending. As this effect is purely geometrical, it becomes critical to reduce it as much as possible. The value of this in-plane bending highly depends on several parameters such as the strut junction distance or the relative wing-strut sweep. Figure 6b illustrates the changes in force and moment distributions when the strut is placed under the wing (as shown by the red lines on the wing image).

The lift bending should not also be neglected as these results show that the maximum bending can be obtained at the root but also at the wing-strut junction where the inertia was much lower for a wing with a single taper, proportionally leading to higher stresses and new critical design locations.

Following those preliminary results, the DoE was defined as explained in Section 2.1, to take into account the effect of the in-plane bending moment and the relative strut sweep with respect to the wing. Though it cannot be fully placed right under the wing because of wing-strut aerodynamic interactions, it cannot either have an important relative sweep angle to prevent introducing an extra predominant internal moment.
Moreover, the internal moment diagrams show that the maximum bending location can also be at the strut-wing junction so more inertia is introduced at this location by designing the double-tapered wing. An inner section with high taper ratio ensures a large chord up to the junction and an outer section with low taper preserves the aerodynamic performance.

2.4 Aerodynamic modelling

In addition to the structural model, an aerodynamic Doublet Lattice Method (DLM) mesh is created. The wing, the vertical tail plane (VTP) and the horizontal tail plane (HTP) planforms are meshed into aerodynamic panels as shown in Figure 7 .



do

Figure 7 – Aerodynamic DLM mesh of the wing, HTP and VTP

Each of these panels calculates a downwash at 3/4 chord from a boundary condition depending on the angle of attack (α_i), the elastic twist angle (θ_i) and the vertical structure velocity (the last being null for static aeroelastic calculations). Each panel contribution is then assembled through the Aerodynamic Influence Coefficient (AIC) matrix and converted into a force [7] [8]. These aerodynamic forces are then interpolated to the structural nodes through splines.

Thus, this method is solely dependent on the true angle of attack ($\theta_i + \alpha_i$) but it only applies to flat shapes. Hence, it does not natively consider profile camber or the initial twist distribution that are key aerodynamic parameters. It is then possible to apply a downwash correction in the form of an extra downwash vector called W2GJ in MSC Nastran.
However, while the camber correction angle can easily be calculated geometrically from the profile center line, the twist correction requires more computations to be predicted.

Indeed, a target twist law is defined by the high fidelity aerodynamics corresponding to the twist of the deformed wing under cruise conditions.
As the structure is flexible, the initial applied twist correction law must be calibrated by an iterative process so that the addition of this applied aerodynamic twist (defining the unknown jig shape) and the elastic twist deformation corresponds to the target twist predicted by the aerodynamics under cruise conditions.
The first step of this process consists in applying only the camber correction and calculating the resulting twist under aeroelastic loads. Secondly, the difference between the target and measured twist is added to the initial applied correction until convergence towards the target twist is achieved to

obtain the jig shape (i.e. an applied twist distribution solving this problem) . This process is shown in Figure 8.

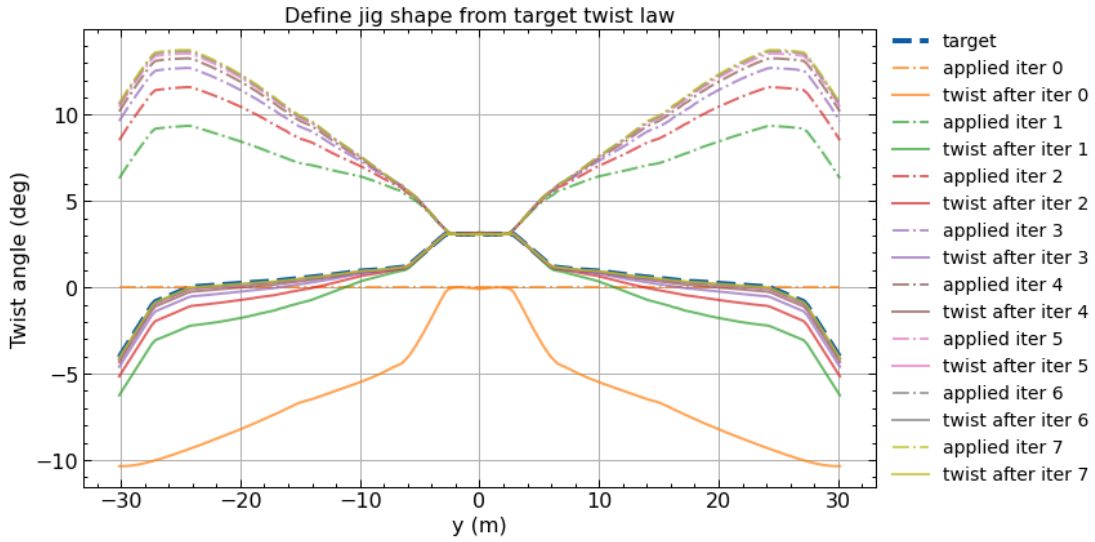


Figure 8 – Results of the twist correction law.
For each iteration, an initial twist correction is applied (dotted lines) and the aeroelastic deformation is calculated (solid lines). The initial twist is updated by subtracting the difference with the aerodynamic cruise target twist law (dashed blue line) . The process should converge towards this target law.

The same correction can be used for other load cases that are not directly computed by the CFD calculations (i.e. -1g, 2.5g load cases).

This modelling can also allow to perform calculations on fluid-structure instabilities such as flutter. Flutter is an instability due to a dynamic fluid-structure coupling. Once a critical velocity is reached, aerodynamics introduce a negative damping of a structural mode which is then amplified and may lead to structure breakdown (for linear flutter).
Flutter is calculated using the p-k method implemented in MSC Nastran to solve equation 3 .

$$\left[M_{hh}p^2 + \left(B_{hh} - \frac{1}{4}\rho\bar{c}VQ^I_{hh}/k\right)p + \left(K_{hh} - \frac{1}{2}\rho V^2 Q^R_{hh}\right)\right]\{u_h\} = 0 \tag{3}$$

where M_{hh}, B_{hh}, K_{hh} are the modal mass, damping and stiffness matrices, $\{u_h\}$ the modal amplitude vector, ρ, V the fluid density and velocity, $\bar{c}$ the reference chord. Q^R_{hh} and Q^I_{hh} are the real and imaginary parts of the modal aerodynamic stiffness matrix, (depending on Mach number and reduced frequency k). $p = \omega(\gamma \pm i)$ (with ω the circular frequency and γ the transient decay rate coefficient) is the eigenvalue of the flutter problem [9].

For a range of Mach numbers, the flutter equation is solved for a set of altitudes (i.e. a (ρ,V) pairs). For each element of this set, a non-linear eigenvalue problem is solved, giving the aeroelastic frequency and damping of each mode. A positive damping indicates flutter from this critical velocity. For example, for the flutter diagrams (damping and frequency evolution with True Air Speed (TAS) for a range of modes) in Figure 9, a light purple mode gets a positive damping for a critical velocity around 640 km/h (178 m/s).

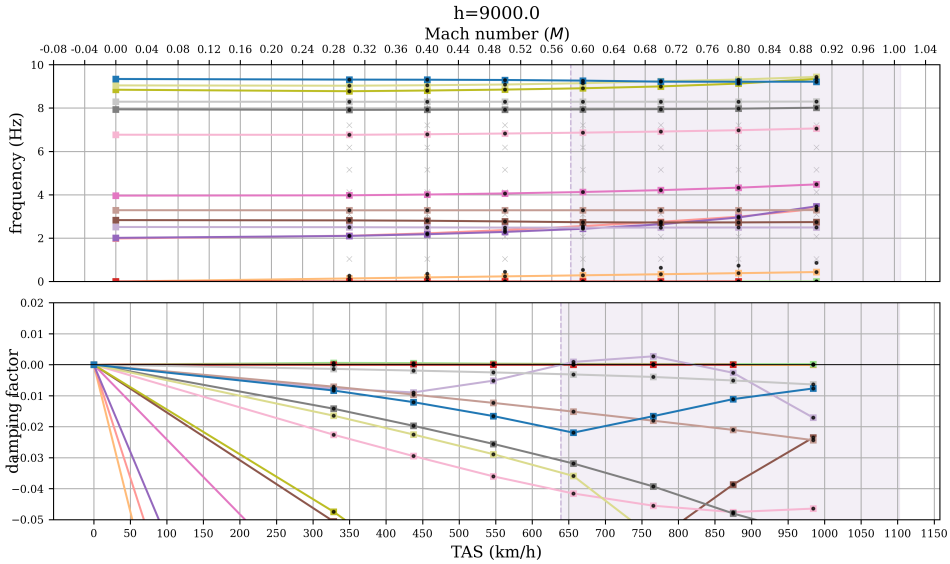


Figure 9 – Flutter diagrams at altitude h $= 9000$m showing a critical flutter velocity of 640 km/h (178 m/s).

Figure 10 shows the flight envelope (ie the (h,V) flying points) for which flutter is to be checked for the SBW. For each (h,V) point marked by a cross, the flutter equation is solved.
The flutter critical velocities obtained by interpolation for each altitude are then added to the flight envelope to define the flutter boundaries (in dotted red lines in Figure 10).
A description of the flight envelope construction can be found in [10]. As flutter must be checked beyond the Maximum Operating Mach number (MMO), the flight envelope is extended up to dive Mach number $M_d \approx MMO + 0.07$.

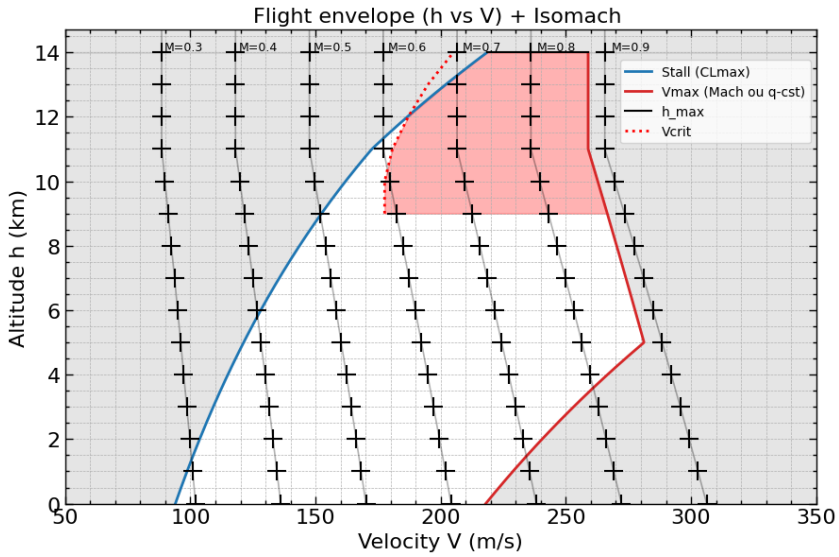


Figure 10 – Example of the flight envelope with iso-Mach curves for a DoE point aircraft with $S_{ref} = 145\,\text{m}^2$, $C_{L\max} = 1$, MTOW $= 80$t, and MMO $= 0.82$. The flutter critical velocity for different altitudes is represented by the red dotted line, and the flutter zone is highlighted in red.

2.5 Load cases

The structural and aeroelastic optimizations can be performed using 2 types of loadcases : Manoeuvre Load Alleviation (MLA) loadcases and trim forces loadcases issued from the aeroelastic angle-of-attack and elevator trim calculations.

The MLA loadcase is designed from a bell shape distribution to which a Load Alleviation Factor (LAF) is applied to consider the load alleviation systems on the load distribution (especially in order to reduce the loading towards the wing tip). Figure 11 illustrates the effect of the LAF on the load distribution: a higher LAF implies that the load is strongly reduced in the wing tip region and thus increased near the wing root. The break in the curve can also be moved spanwise though this parameter is fixed in the DoE process.

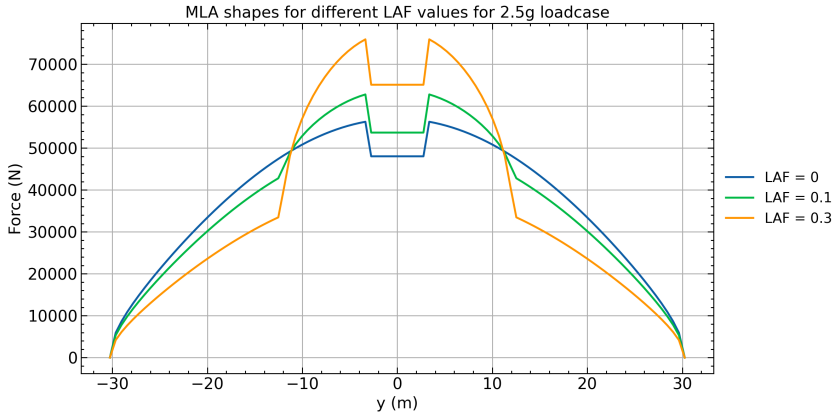


Figure 11 – Illustration of the effect of the LAF parameter on the MLA

This load shape should then be transformed into a set of forces to apply on each structural loading node, located at the quarter chord of each rib. The lift force for each bay is integrated over the bay length, and then distributed over its adjacent ribs according to the local lift's distribution centroid. Thus, each rib sees a summation of the right and left contribution from the lift bay force. As the bay length may vary a lot near the strut-wing junction, the loading distribution can be locally discontinuous as it can be observed in Figure 12.

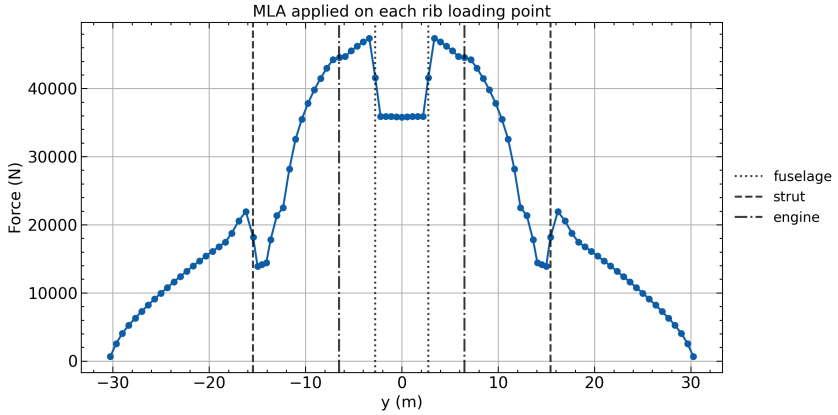


Figure 12 – Forces applied on each bay (represented by a blue dot) for a 2.5g loadcase with LAF=0.3

The static aeroelastic analysis is performed using MSC NASTRAN SOL 144 by calculating the wing and HTP elevator trimmed angle of attack given the total loading (1g for example). This results in a set of trim forces that can be applied for the structural design.

In this paper, two load combinations can be used independently :

Load case	1G	-1G	2.5G
Structural optimizations	MLA0	MLA0	MLA
Aeroelastic optimizations	DLM Trim	DLM Trim	MLA

Table 2 – Summary of the load calculation method for structural and aeroelastic optimizations (MLA0 is MLA loading with LAF=0 and DLM Trim forces are obtained using MSC Nastran SOL 144)

The LAF applied for the 2.5G case is a parameter of the global DoE and thus can vary within the DoE range (see Table 1) for different aircraft configuration.

2.6 General optimization process

The main mass minimization, performed using MSC Nastran SOL 200, is nested in a global optimization process in order to estimate the optimized mass as illustrated by Figure 13. After generating the model from the surrogate information to build the aircraft corresponding to a given DoE point, each structural design variable is given an initial value. A fully stress calculation (SOL200_fs) can optionally be performed to refine the starting point of the optimization process.
The main optimization calculation (SOL200) is performed by minimizing the wing and strut primary structure mass under both stress and global buckling constraints according to the loadings described in Table 2. The DLM trim forces computation (via SOL144) requires an update in the camber and twist downwash correction at each iteration to match the cruise shape as detailed in Section 2.4.
The MLA loading is updated so the total loading for both trim cases and MLA cases are computed from the actual MTOW.
The model properties are then adjusted based on the final design variables values. Post checks are performed to compute the final mass and constraint violation, and verify flutter.

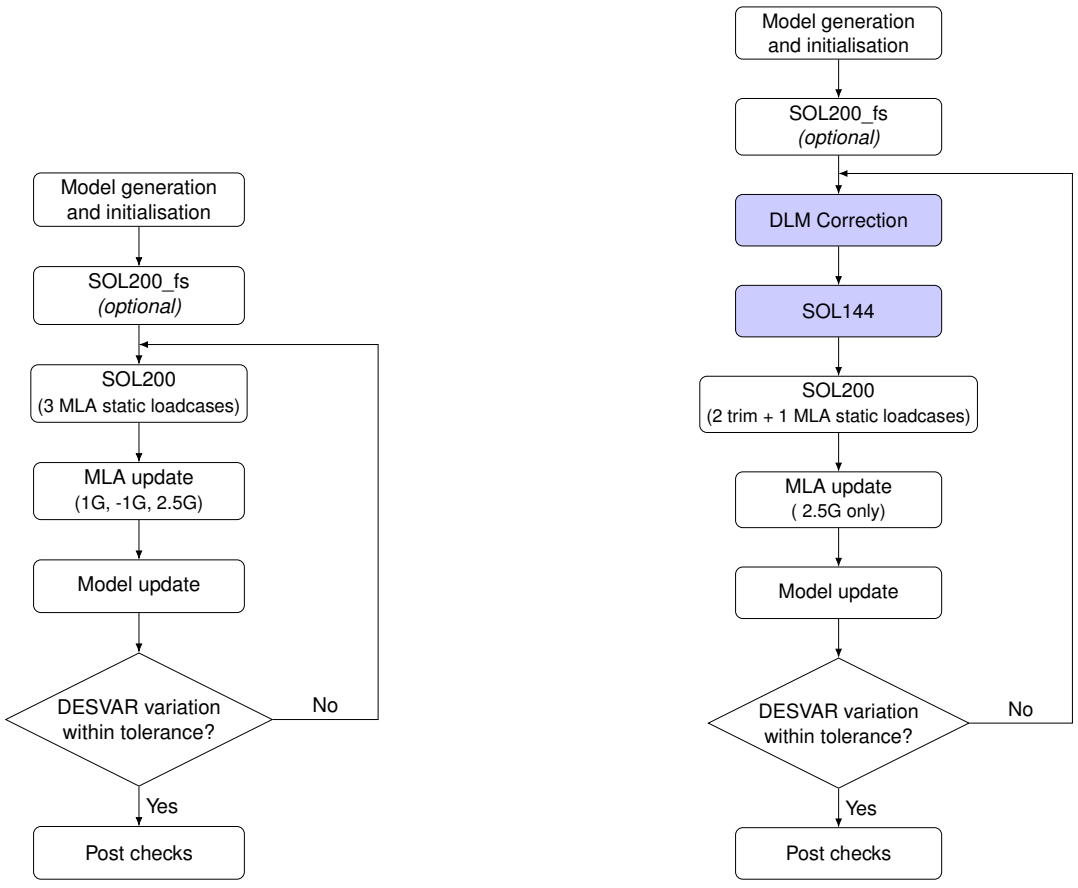


Figure 13 – Optimization process used for structural and aeroelastic optimizations

This process finally returns a primary mass for the wing, the strut and eventually for a jury strut if relevant. This mass is then sent to the MDO process to build the surrogate model.
After several iterations of aircraft evaluations for the MDO process, the best aircraft configuration in terms of block fuel is selected.

3. Results

3.1 Configuration selected from the structural optimization process

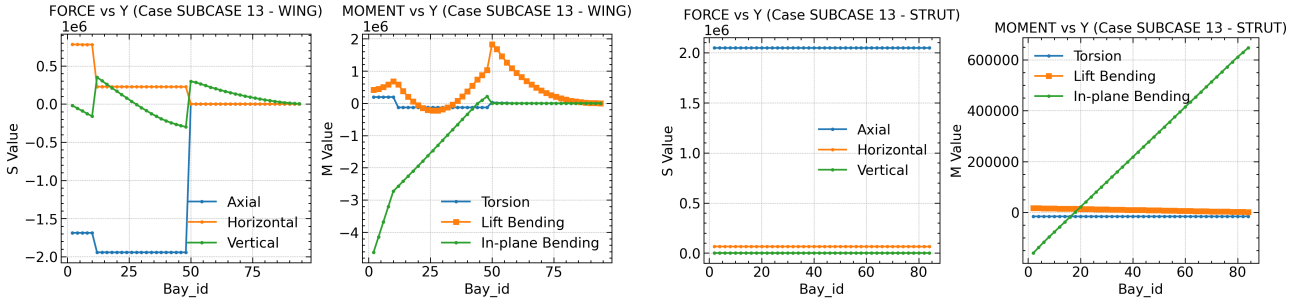
3.1.1 Description of the optimized configuration

With the stuctural and CFD high fidelity improved surrogate model with several feedback loops, the MDO process led to an optimal configuration in terms of block fuel minimization. Its geometry and performance are described below.

Part	Design Variables	Optimal	Range
WING	Aspect Ratio AR	22.91	15 - 28
	Wing sweep at 25% chord (°)	23.64	20.0 - 27.5
	Root relative thickness $t/c_{\text{wing root}}$	0.105	10 % - 13 %
	Kink relative thickness $t/c_{\text{wing kink}}$	0.110	10 % - 13 %
STRUT	Relative thickness t/c_{strut}	0.107	10 % - 13 %
	Root chord $c_{\text{strut root}}$ (m)	1.115	1 - 4
	Wing/Strut junction Y_{strut} (% wing semi-span)	0.48	30 % - 60 %
	Wing/Strut relative sweep angle (% wing sweep angle)	0.658	10 % - 100 %
LOAD	Load alleviation factor LAF	0.281	0.001 - 0.3

Table 3 – Values of the parameters for the optimal configuration issued from the DoE

This configuration has achieved a high aspect ratio with a strut junction located around the half semi-span to sustain efficiently the wing loads without having buckling or stress issues in the strut itself. Hence, from a structural point of view, a relatively thin and small strut is obtained with dimensions closed to the lower bounds which is because the strut mainly works in traction/compression so the cross-section is more important than the inertia (see Figure 14) for structural resistance. The influence of these parameters on the aircraft performance is indeed more driven by the aerodynamic considerations.
The wing thickness ratio is more important at the kink (i.e. near the wing-strut junction) than at the root because it compensates the higher wing lift bending moment at this position. The LAF is at the highest possible which reduces the load at the wing tip but this value must yet be achieved by a design of the control surfaces.



(a) Wing (b) Strut

Figure 14 – Force and Moment diagrams for the wing and strut of the optimal configuration under 2.5g MLA loads

Looking at the efforts along the wing, two parts can be defined : an outer wing that behaves as a cantilever and an inner wing that looks more like a double-supported beam. However, as shown in Section 2.3, the strut also introduces new efforts including :

- An axial force in the inner wing.
- A drop in wing lift bending moment at the junction due to its clamped connection.
- And an in-plane bending moment in the inner wing because the optimal wing/strut relative sweep angle variable is not 100% which is a result from the compromise with the aerodynamic performance.

But this last in-plane moment is highly compensated by the inertia I_{zz} so the dominant term in the σ_{worst} equation (2) is the second one depending on the lift bending .
An image of the optimized configuration compared with the initial design [3] is shown in Figure 15 :

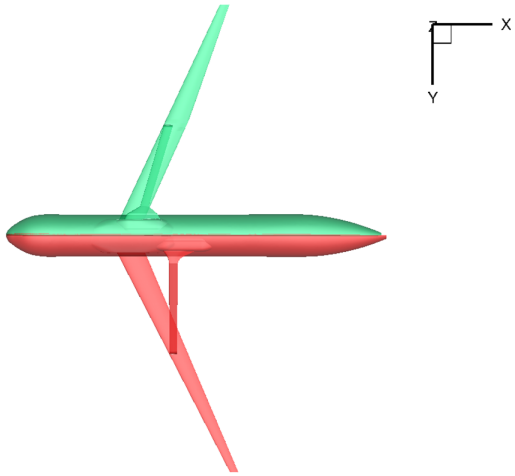
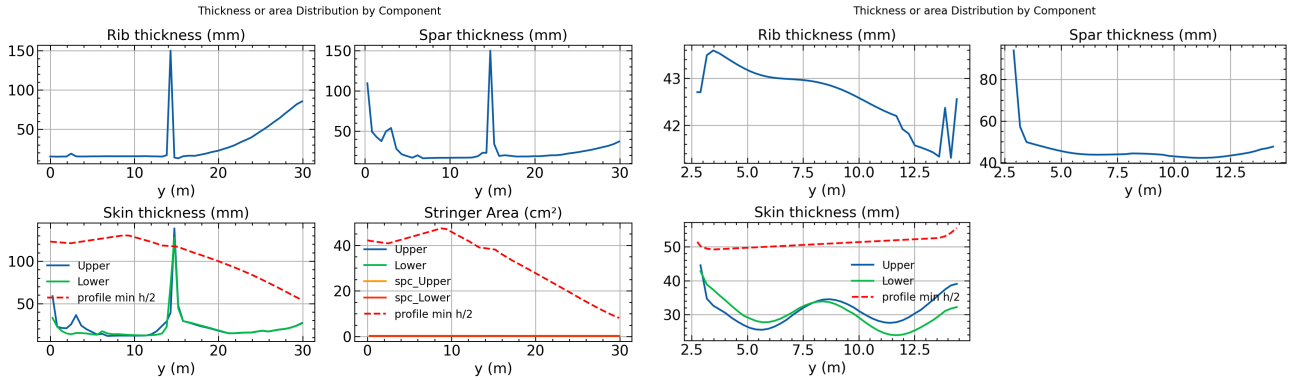


Figure 15 – Comparison of the optimized design (in green) and the initial design (in red)

The main tendencies of the optimization include a wing with higher inertia at the junction and a strut more aligned under the wing.

3.1.2 Structural evaluation

After structural optimization of the selected configuration, the thickness distributions for the wing and the strut are obtained and displayed in Figure 16 for the main components. The mass breakdown for each bay of the wing is in Figure 17.



(a) Wing (b) Strut

Figure 16 – Optimized thicknesses for the wing and strut components on the optimal configuration

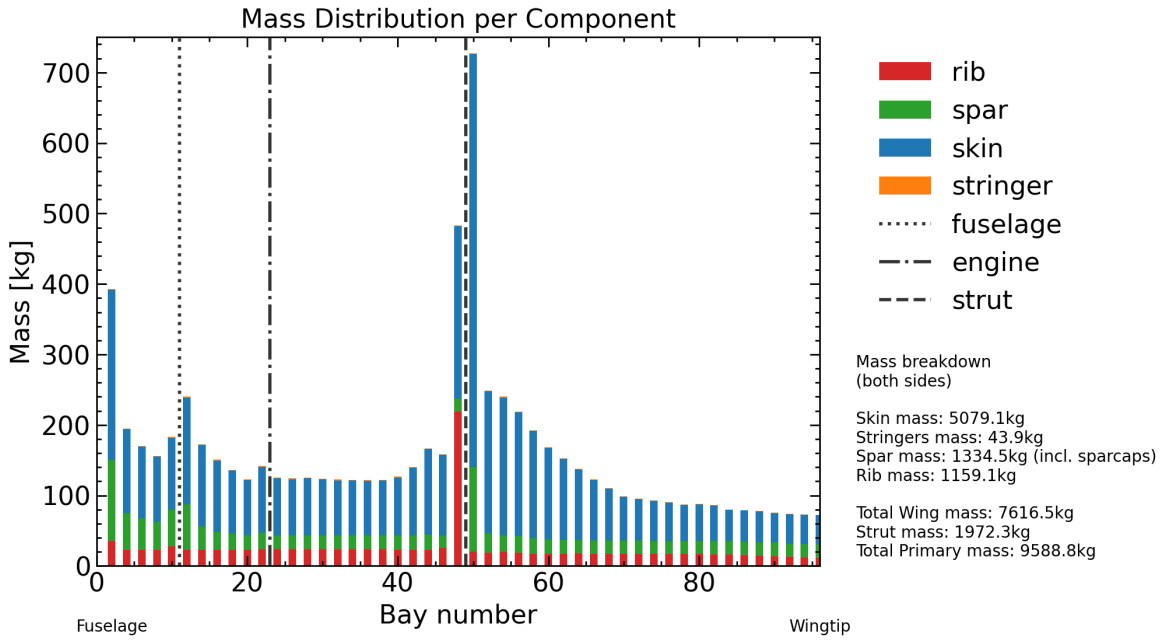
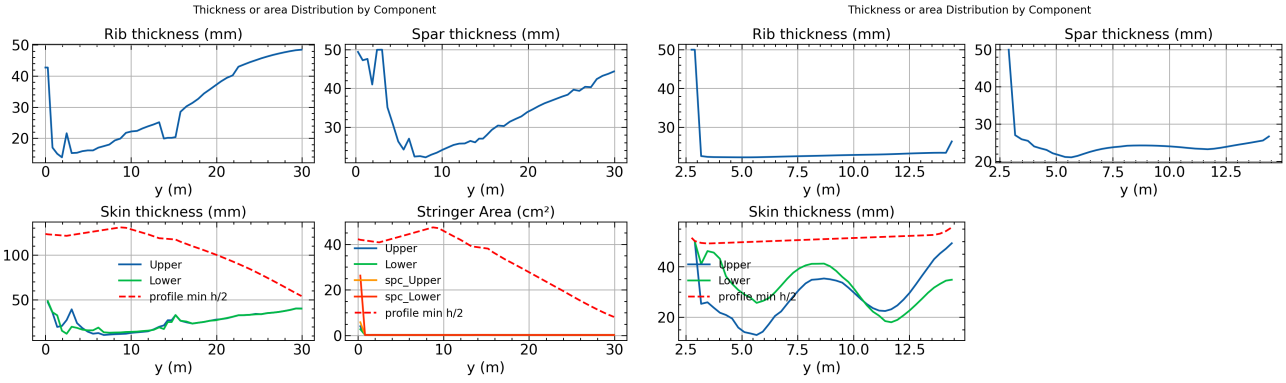


Figure 17 – Mass breakdown per bay for the wing of the optimal configuration

These results show that the wing primary mass is mainly driven by the skins which take most of the lift bending loads.
The mass distribution also has a similar shape as the lift bending diagram (Figure 14a), and most of the material is added just after the strut junction (which would correspond to the root of the cantilever outer wing) because this is the section where there is the most bending moment and where the wing-box dimensions start to be reduced by the wing geometry. To ensure the local stress concentration due to the rigid connection do not excessively impact the surrogate model, the optimization bounds were increased for robustness. However, the thickness obtained at the junction exceeds largely the profile height. So this configuration is not directly manufacturable.
A second optimization has been performed with tighter bounds to ensure the limits are respected. The strut-wing junction bays are excluded of the optimization constraint under the assumption that a detailed design on the junction mechanisms must be carried out separately and that the local over constraints due to having a perfectly rigid link are not physically representative. The resulting strut-braced wing has an increase in primary mass of around 325 kg and respects the profile limits. Its thickness distribution and mass breakdown are displayed in Figure 18 and 19.



(a) Wing (b) Strut

Figure 18 – Optimized thicknesses for the wing and strut components on the optimal configuration with a 5cm maximum thickness allowed

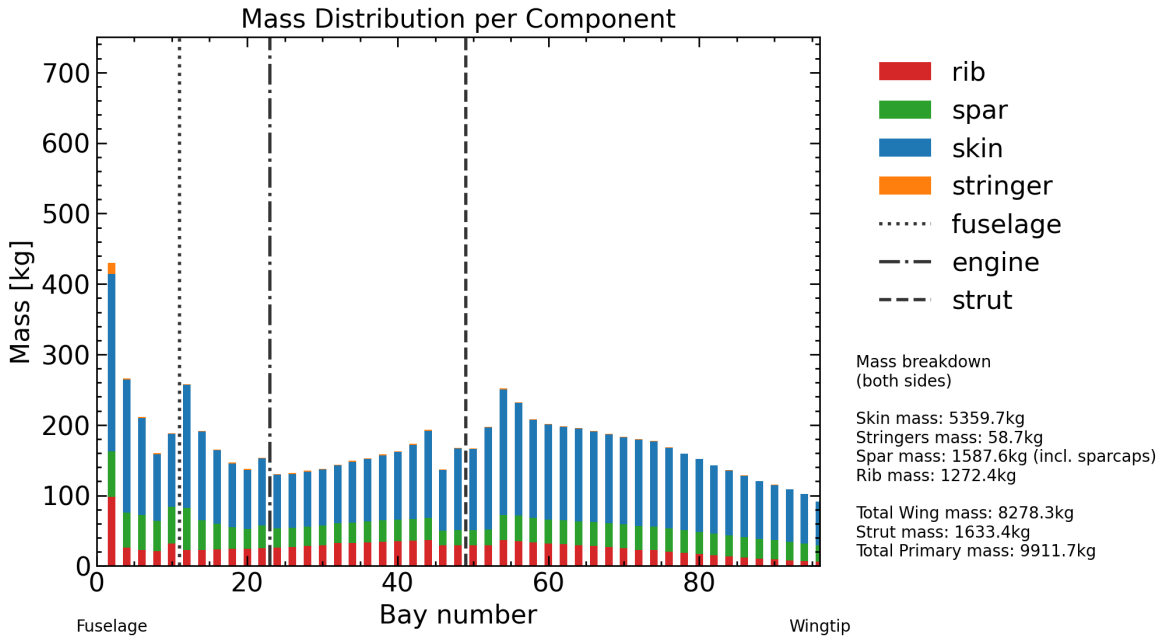
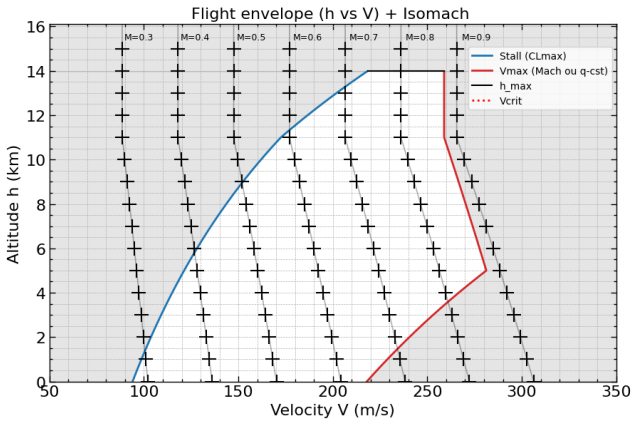


Figure 19 – Mass breakdown per bay for the wing of the optimal configuration with a 5cm maximum thickness allowed

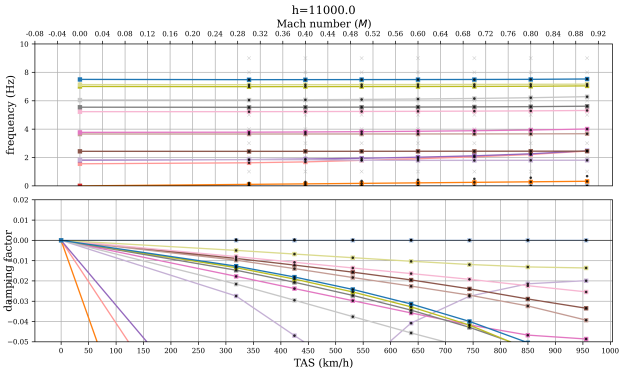
The mass distribution shows a similar pattern as the one in Figure 17 and the peak due to the junction does not appear anymore but the wing tip bays are thicker. Indeed, the thickness plots indicate that the rib and spar thicknesses tend to increase towards the wing tip which is counter-intuitive. This could be explained by the fact that - as the thickness can not longer be increased at the outer wing root - the optimization chooses to stiffen the wing tip to reduce the maximum tip displacement and thus the stress caused by the given efforts. The maximum tip displacement is 2.30m under 2.5g load case with the large bounds and 1.95m with the tighter bounds. Another explanation would be that the optimization is trapped in a local minimum and that the mass could indeed still be reduced by searching for a thinner design on the wing tip.

3.1.3 Flutter

Flutter was also checked and no flutter mode was observed around the flight envelope as shown in Figure 20 :



(a) Flight envelope



(b) Flutter diagram at cruise altitude (h=11000m)

Figure 20 – Flutter results on optimal configuration.
No flutter was detected for the considered flight conditions.

3.2 Load evaluation using DLM

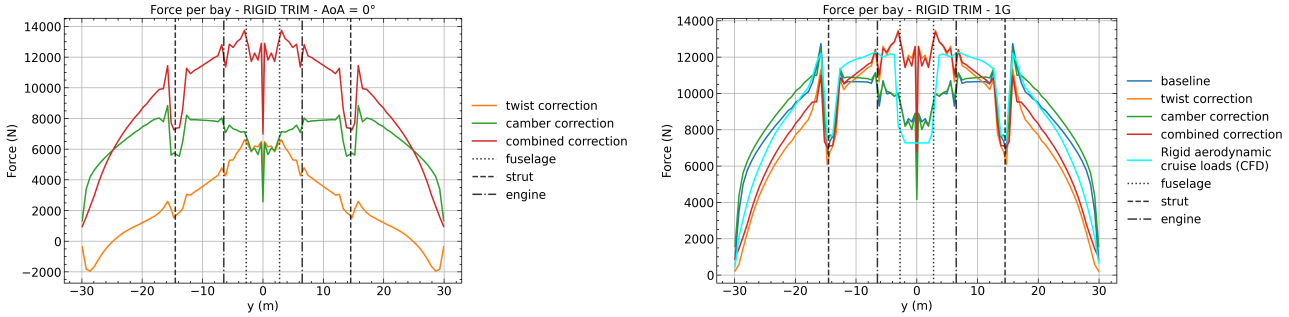
The design process with a structural optimization has converged to an optimal configuration able to sustain MLA loadings.
Now it is also necessary to search for an optimum by considering the aeroelastic loads. As described in section 2.4, the aeroelastic loading is obtained from a DLM calculation under trimmed conditions. They are then compared with Reynolds Average Navier Stokes (RANS) CFD calculations.

3.2.1 Rigid Wing

In order to be able to compare the loads from the DLM to the rigid wing CFD calculations, the structure was stiffened by using a fake material wing with a Young modulus $E = 1e15$ Pa. From this rigid wing, two trim calculations were performed to evaluate the effect of different DLM corrections (profile camber, aerodynamic twist applied and a combined correction considering both effects) :

- A trim at $\alpha = 0.0°$, with load factor n_z free, to isolate the contribution of the correction alone.
- A trim at $n_z = +1$, with α free, to plot the actual loading under 1g cruise condition for a trimmed aircraft.

The results from both calculations are displayed in Figure 21.



(a) fixed $\alpha = 0°$ (b) fixed $n_z = +1$

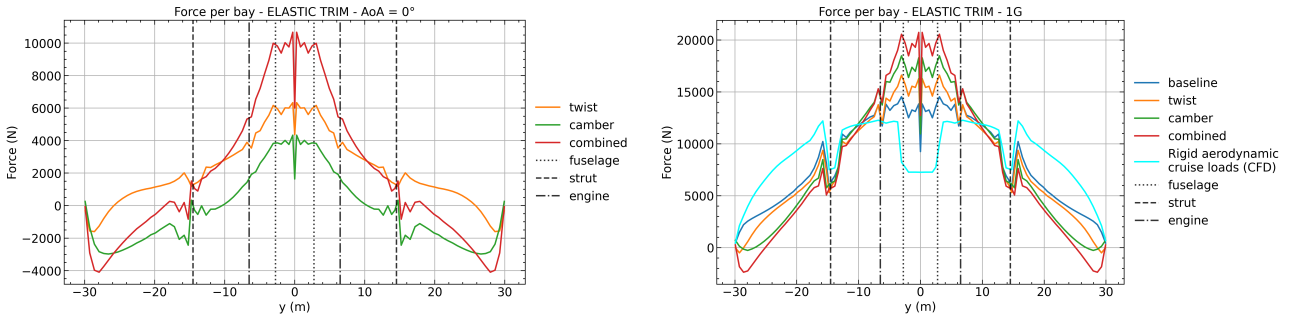
Figure 21 – Load distribution along the span of the rigid optimal configuration.
Results are displayed with no correction (baseline), camber or twist correction, or both corrections and compared to RANS CFD aerodynamic loads.

These results show that, for a rigid wing, the camber correction increases the load almost uniformly along the span while the twist correction designed by the aerodynamics reduces the load towards the wing tip to increase it near the root (see Figure 21a).
In the meantime, Figure 21b illustrates that the overall correction (in red) is more influenced by the twist law applied and, for a rigid wing, the corrected law is clearly closer to the aerodynamic correction than the uncorrected DLM (baseline). This corrected law could be applied to other load cases to mimic the CFD calculation at a lower computation time.

3.2.2 Flexible wing

However, for the structural optimization, the wing is not fully rigid. This means that the wing flexibility should be taken into account. Indeed, the wing deformation, especially in terms of twist deformation (θ) influences the flow and this interaction is considered by the DLM through the splines. This leads to a flexible trim angle angle of attack $\alpha_{\text{flexible}} \neq \alpha_{\text{rigid}}$. The same two calculations performed for a rigid wing were implemented on the true flexible wing and load distributions are given in Figure 22.

https://doi.org/10.71945/icas2026_0342



(a) fixed $\alpha = 0°$ (b) fixed $n_z = +1$

Figure 22 – Load distribution along the span of the flexible optimal configuration.
Results are displayed with no correction (baseline), camber or twist correction, or both corrections and compared to RANS CFD aerodynamic loads.

Figure 22a illustrates that the wing flexibility tends to reduce the wing tip loading induced by the camber correction. In fact, the profile camber will induce more wing de-twisting and thus a reduction of the apparent angle of attack $(\alpha + \theta)$. This leads to a reduction of the load for the most flexible parts of the wing (i.e. the wing tip section). The twist correction is not impacted by the flexibility effect but the total combined correction is.
For a +1g trim (Figure 22b), the flexibility effect is thus mainly to unload the wing tip. However this leads to a completely different load distribution than the one predicted by the rigid aerodynamics. To match this aerodynamic load, the initial applied twist must be adapted so that the loads issued from the combined correction get closer to the aerodynamic target load under cruise conditions.

3.2.3 Target twist loads

For the aeroelastic design, the DLM is used to get representative aerodynamic loads with a low computing cost to be applied on several flight conditions and consider the wing flexibility. Nevertheless, the CFD calculation is performed on a rigid wing only.
To match the aerodynamic design cruise shape with a flexible wing, the target twist process described in Section 2.4 is implemented to find the initial applied twist correction for which the combined correction matches with the CFD loads.
The result of this process on the optimized configuration appears in Figure 23.

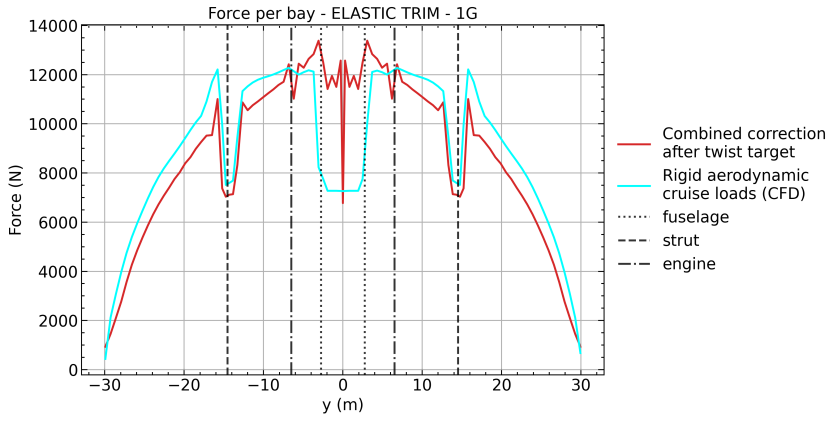


Figure 23 – DLM loads obtained after the target twist computation compared with loads from CFD in cruise conditions.

This target twist process results in more representative loads than the original DLM loads. However, a few distinctions can be noted.
First, the fuselage is not represented in the DLM modelling so its contribution does not appear in the load plot. It could be modelled in MSC Nastran using slender bodies for example.

Secondly, the load on the outer part of the wing is slightly underestimated compared with the CFD. Indeed, the DLM does not take into account the transonic effects that are considered in the RANS calculations. Yet, the transonic effects tend to increase the loads in the regions where the lift coefficient c_L is he most important. This may explain the differences in loading observed on the outer part of the wing.
The load is considered here representative enough of the CFD to perform an aeroelastic optimization for a new DoE using this process.

4. Conclusion and future work

In conclusion, this paper presents the work carried out for the structural design of a Strut-Braced Wing (SBW) with ultra high aspect ratio for a hydrogen Short-Medium-Range commercial aircraft.
It illustrates the structural optimization process used to minimize the primary mass of such aircraft and its role in the global Multi-disciplinary Design Optimization (MDO) process. Thus, the structural optimization has demonstrated the preeminent influence of some parameters such as the relative wing-strut sweep in the design process. Essential geometry adaptations were also exposed in order to ensure enough structural inertia is available at the wing-strut junction using a double-tapered wing. Through these structural optimizations, the MDO process has been provided wing and strut primary masses for a set of Design of Experiments (DoE) points that led to the constitution of a surrogate model and the selection of an optimized SBW configuration presented in Section 3.1.1. This 22.91 aspect ratio aircraft was then checked for its ability to resist the design load cases and also not to enter into flutter within its flight envelope. However, it has also needed an extra optimization step to correct unrealistic thickness at some locations, for instance near the strut-wing junction and it does not yet consider aeroelastic loads.

Hence, future work includes the use of the aeroelastic optimization process to achieve an even more realistic configuration accounting for the wing flexibility effect on the load distribution by using the target twist process in the optimization. Also, a full high fidelity aeroelastic performance evaluation using coupled Computationnal Fluid Dynamics (CFD) and structural calculations could be performed. The structural modelling is also to be refined by studying the junction mechanism, for example by considering a simple or a double pivot joint at the junction as illustrated in [11]. The detailed mechanism design though remains out of the scope of this work and the wing bays around the junction can be removed from the optimization process to ensure smoother thickness distributions.
The optimization process can also be reconsidered, especially for a change in the objective function as the OWE includes a set of non-structural masses that dilutes the effect of a change of wing primary mass on the gradients. Tighter bounds for the design variables can also be implemented to prevent any thickness overshoot to happen.
Moreover, the addition of a jury strut to reduce the buckling impact on the design can also be studied as some studies have demonstrated global performance improvements [12].
Finally, this work can be completed by studying the effect of considering composite material instead of black aluminium and the use of dry wings (i.e. without fuel within the wingbox) opens new layout possibilities to explore through topology optimization [5].

5. Acknowledgement

The Ultra Performance Wing (UP Wing, project number: 101101974) and SMR ACAP (project number: 101101955) projects are supported by the Clean Aviation Joint Undertaking and its members, co-funded by the European Union. The views and opinions expressed are however those of the authors only and do not necessarily reflect those of the European Union or Clean Aviation Joint Undertaking. Neither the European Union nor the granting authority can be held responsible for them.





Co-funded by the European Union

6. Contact Author Email Address

charly.mollet@onera.fr; lander.vertonghen@onera.fr; cedric.julien@onera.fr

7. Copyright Statement

The authors confirm that they, and/or their company or organization, hold copyright on all of the original material included in this paper. The authors also confirm that they have obtained permission, from the copyright holder of any third party material included in this paper, to publish it as part of their paper. The authors confirm that they give permission, or have obtained permission from the copyright holder of this paper, for the publication and distribution of this paper as part of the ICAS proceedings or as individual off-prints from the proceedings.

References

[1] Yiyuan Ma and Ali Elham. Designing high aspect ratio wings: A review of concepts and approaches. *Progress in Aerospace Sciences*, 145:100983, 2024.

[2] Gérald Carrier, Guillaume Arnoult, Nicolo Fabbiane, Jean-Sébastien Schotté, Christophe David, Sébastien Defoort, Martin Delavenne, and Emmanuel Bénard. Multidisciplinary analysis and design of strut-braced wing concept for medium range aircraft. In *AIAA SciTech 2022 Forum*, San Diego, United States, jan 2022.

[3] M. Méheut, D. Losada Costoso, F. Moens, O. Atinault, C. Julien, L. Vertonghen, L. Coelho, V. Priasso, A. Lannoo, S. Defoort, E. Nguyen Van, C. David, D. Glenis, J. Sodja, S. de Boer, J. Schwingel, and D. Eisenhut. Strut-braced dry wing concept for hydrogen-powered aircraft. In *34th Congress of the International Council of the Aeronautical Sciences (ICAS 2024)*, Florence, Italy, sep 2024. International Council of the Aeronautical Sciences.

[4] Enrico Stragiotti, Eric Nguyen Van, Romain Parello, Sebastien Defoort, Diego Losada Costoso, Charly Mollet, Michaël Méheut, Olivier Atinault, Frédéric Möens, Lander Vertonghen, Cédric Julien, Antoine Lannoo, and Valentin Priasso. Swift: A ultra high aspect ratio strut-braced dry wing hydrogen-powered aircraft. In *Proceedings of the 35th Congress of the International Council of the Aeronautical Sciences (ICAS 2026)*, Sydney, Australia, September 2026. International Council of the Aeronautical Sciences.

[5] Lander Vertonghen, Charly Mollet, Cédric Julien, and François-Xavier Irisarri. Combined topology and composite laminate optimization of a strut-braced dry wing for a hydrogen aircraft. In *35th Congress of the International Council of the Aeronautical Sciences (ICAS 2026)*, Sydney, Australia, sep 2026. International Council of the Aeronautical Sciences.

[6] Christopher Szczyglowski. *Passive Aeroelastic Control in Truss-Braced Wings using Vibration Suppression*. PhD thesis, 04 2020.

[7] Maxwell Blair. A compilation of the mathematics leading to the doublet lattice method. 1992.

[8] Edward Albano and William P. Rodden. A doublet lattice method for calculating lift distributions on oscillating surfaces in subsonic flows. *AIAA Journal*, 7(2):279–285, February 1969.

[9] H. J. Hassig. An approximate true damping solution of the flutter equation by determinant iteration. *Journal of Aircraft*, 8(11):885–889, 1971.

[10] Antonio Filippone. *Advanced aircraft flight performance*, volume 9781107024007. Cambridge University Press, 2010.

[11] Neal A. Harrison, Krishna Hoffman, David S. Lazzara, Eric Y. Reichenbach, Anthony J. Sclafani, and Christopher K. Droncy. Subsonic ultra green aircraft research: Phase iv final report – volume i: Mach 0.80 transonic truss-braced wing high-speed design report. NASA Contractor Report NASA/CR-20220016017 Volume I, National Aeronautics and Space Administration, Hampton, Virginia, oct 2023.

[12] Yiyuan Ma, Yongqi Du, Yue Wang, Keshi Zhang, and Zhonghua Han. Aerostructural comparative study of composite strut- and truss-braced wing configurations. *Journal of Aircraft*, oct 2025. Published Online: 23 Oct 2025.